Journal for Multiscale Computational Engineering, 10 (5): 391–405 (2012)

APPLICATION OF A MULTISCALE COHESIVE ZONE METHOD TO MODEL COMPOSITE MATERIALS

Xiaowei Zeng[1,2] *& Shaofan Li*[1,*]

[1]*Department of Civil and Environmental Engineering, University of California, Berkeley, California 94720, USA*

[2]*Department of Mechanical Engineering, University of Texas, San Antonio, TX 78249, USA*

[*]Address all correspondence to Shaofan Li E-mail: shaofan@berkeley.edu

One of the major problems in failure analysis of composite materials is how to accurately describe interfacial material properties and related interface constitutive modeling at the nanoscale, mesoscale, and macroscale. In this work, we have applied a recently developed multiscale cohesive zone method to model composite materials and, subsequently, we have simulated the failure process of laminar composites. We have shown that the multiscale cohesive zone method can adequately describe mesoscale interface material properties such as interface strength, microstructures, and possible defects or damage. Moreover, we have applied the multiscale cohesive zone model to simulate spall fracture in composite materials induced by high-speed impacts. Simulations of different fracture patterns for composite materials with defects are also presented.

KEY WORDS: *cohesive zone model, composite materials, finite-element method, fracture, impact, multiscale simulations*

1. INTRODUCTION

Strength-based failure criteria are commonly used to predict failure in composite materials. A large number of continuum-based criteria have been proposed in the past to relate stresses and experimental measures of material strength to the onset of failures. For composite structures that can accumulate damage before structural collapse, the use of failure criteria is not sufficient to predict ultimate failure. In order to attain satisfactory accuracy and to capture the basic characteristics of quasi-brittle fracture of a laminate composites, detailed fracture mechanics simulation and analysis are necessary.

As early as the 1970s, people started using crack-band-type or cohesive zone-type finite elements to simulate fractures in composite materials such as laminar plates and reinforced concretes (e.g., Hillerborg et al., 1976). One may find the recent developments on cohesive finite-element methods in Matous et al. (2008), Alfaro et al. (2009, 2010), and Samimi et al. (2009). One of the current trends in cohesive finite element research is to develop multiscale cohesive zone model to simulate fracture and damage in composite materials (e.g., Hirschberger et al., 2009; Geers et al., 2010). The cohesive laws derived in the above literature are essentially empirical cohesive formulations, and the term multiscale is used in only the sense as a multiscale mathematics paradigm. In fact, it has been public consensus now that the ideal approach or the best way to form a truly reliable cohesive law is to extrapolate constitutive information from atomistic microstructures (see Nguyen and Ortiz, 2002; Hayes et al., 2004; Braides et al., 2006).

Following a multiscale approach, in this work, we apply a newly developed multiscale cohesive zone model (MCZM) (Zeng and Li, 2010) to model the composite materials and simulate their failure process. There are several advantages in applying the MCZM to study composite materials: (1) composite material is very easy to model by using the MCZM, because it can precisely model each individual phase or component corresponding to their atomistic constituents; (2) the MCZM provides a very accurate description for interface material properties at the mesoscale; and (3) the MCZM provides naturally a material frame-indifference or objective interface failure criterion so it may

1543–1649/12/$35.00

finally resolve the outstanding problem of how to model the mixed-mode fracture and damage by employing the cohesive zone finite-element methods.

The paper is organized in five sections: in Section 2 we shall review the MCZM; and Section 3 is focused on finite-element implementation of the cohesive zone model. In Section 4 we shall discuss the mixed-mode cohesive law. In Section 5 we study the mesh sensitivity of the multiscale cohesive zone method. A few numerical examples are presented for composite materials modeling and simulations in Section 6 and, finally, we shall conclude thea current study in Section 7.

2. A MULTISCALE COHESIVE ZONE MODEL

In a recent work (Zeng and Li, 2010), the present authors have proposed and implemented a MCZM. In this method, there are two coarse graining models: one for bulk medium and another for material interfaces, or defects (e.g., persistent slip band). By constructing a finite width cohesive zone and extending the Cauchy–Born rule to the coarse scale deformation field, the MCZM can simulate the overall behaviors of a non-uniform deformation caused by defects. With the aid of the multiscale cohesive zone method, it is much easier and more efficient to study composite materials with full consideration of microstructure characteristics. There are three major technical ingredients in the MCZM: (a) development of interfacial potential; (b) effective deformation gradient in the cohesive zone; and (c) the Cauchy–Born rule for effective field.

2.1 Development of interfacial potential based on colloidal physics

Modeling the weak interface in composite materials has been a challenge. In most engineering applications, empirical damage or plasticity laws have been used in practice. Most of them are numerical adoptions of the Dugdale–Barenblatt model (Dugdale, 1960; Barenblatt, 1962). Xu and Needleman (1994) provided both cohesive laws in Modes I and II, in which the Mode II cohesive law is an empirical modeling of atomistic potential. However, there are only few mixed-mode cohesive zone models (e.g., Park et al., 2009). Usually, in composite material study, how to relate the parameters of the cohesive zone model with the measurable experimental data appears to be another challenge or an often frustration.

In this work, we propose to employ the MCZM to provide constitutive modeling of the cohesive interface. To characterize such a decohesion mechanism in the interlaminar interface at the mesoscale, we use a generalized depletion potential that has been extensively used in colloidal physics to represent the damaged cohesive strength inside the chosen cohesive zone.

To obtain the depletion potential in the cohesive zone, we assume that the damaged cohesive zone is a compliance interface, and it is much weaker than the adjacent bulk elements. This is because most covalent bonds, metallic bonds, or ionic bonds may have been degenerated to non-covalent bonds, and the intermolecular interaction inside the damage cohesive zone can be described by the van der Waals interaction. The cohesive strength of the cohesive zone can then be determined by the intermolecular forces in surrounding the bulk medium. Under these assumptions, when we calculate the interaction between two material points inside the cohesive zone and the bulk medium, we may consider that the bulk medium is rigid with almost no deformation, so the two bulk elements adjacent to the compliant cohesive zone may be viewed as two rigid body half-spaces.

If the atomistic potential for a given bulk medium is available, which can be a pairwise potential or many-body potentials such as the embedded atom method (EAM) (Daw and Baskes, 1984), we can obtain the atomistic potential of the cohesive zone by integrating the bulk potential over the rigid bulk medium half-space. For instance, if the Lennard–Jones (LJ) potential is chosen as the bulk potential shown in Eq. (1), a coarse graining interface potential can be obtained by analytical integration (see Israelachvili, 1992):

$$\phi_{\text{bulk}} = 4\epsilon \left[\left(\frac{\sigma}{r}\right)^{12} - \left(\frac{\sigma}{r}\right)^{6} \right] \tag{1}$$

$$\phi_{\text{depl}}(r) = \int_{\text{Half Space}} \phi_{\text{bulk}}(r - r')dV' = \frac{\pi\epsilon}{\sqrt{2}} \left[\frac{1}{45} \left(\frac{r_0}{r}\right)^{9} - \frac{1}{3} \left(\frac{r_0}{r}\right)^{3} \right] \tag{2}$$

where ϵ is the depth of the potential well, σ is the (finite) distance at which the bulk atomistic potential is zero; and $r_0 = \sigma 2^{1/6}$ is the equilibrium bond distance in the bulk material.

2.2 Effective Deformation Gradient in the Cohesive Zone

In order to represent possible non-uniform local deformation fields caused by the presence of defects, we first remodel the material interface as a finite width compliance cohesive zone, which is the weakest link in an otherwise homogeneous medium. A primary assumption of this work is that the global non-uniform deformation field may be represented by a piece-wise uniform deformation field that consists of the bulk element of uniformed deformation, and they are connected together by finite-width cohesive zones with highly non-uniform deformation. To quantitatively deal with the non-uniform deformation inside the finite-width cohesive zone, it is then assumed that the non-uniform deformation is multiscale in character; i.e., the displacement field inside the cohesive zone may be written as

$$\mathbf{u} = \bar{\mathbf{u}} + \mathbf{u}' \tag{3}$$

where $\bar{\mathbf{u}}$ is the coarse scale displacement field, which may be also called as the Taylor displacement field; whereas $\mathbf{u}'$ is the fine scale displacement fluctuation field. Using Eq. (3), one may write

$$\mathbf{x} = \mathbf{X} + \mathbf{u} = (\mathbf{X} + \bar{\mathbf{u}}) + \mathbf{u}' = \bar{\mathbf{x}} + \mathbf{x}^{'} \tag{4}$$

where $\bar{\mathbf{x}} = \mathbf{X} + \bar{\mathbf{u}}$ and $\mathbf{x}' = \mathbf{u}'$.

Since inside the cohesive zone the deformation is non-uniform, we may separate the total deformation into different scales, and the spatial deformation gradient in the coarse scale will change far more slowly than that of the fine scale fluctuation field. This may allow us to apply the Cauchy–Born rule to the coarse scale field.

Using a computational homogenization technique, we may represent the general deformation field as

$$\mathbf{x} = \mathbf{F}^c\mathbf{X} + \mathbf{u}^{'} \tag{5}$$

where $\mathbf{F}^c$ is the coarse scale deformation gradient that can be determined by the boundary data along the cohesive zone:

$$\mathbf{F}^c = \frac{1}{|\Omega_0|}\int_{\partial\Omega_0} \mathbf{x} \otimes \boldsymbol{\mathcal{N}} dS \tag{6}$$

Since the boundary of a cohesive zone is also the boundary of the adjacent bulk elements, on the boundary of each cohesive element the fine scale fluctuation displacement filed should vanish, by which we postulate that the following weak condition for fine scale displacement field,

$$\int_{\partial\Omega_c} \mathbf{u}' \otimes \boldsymbol{\mathcal{N}} dS = 0 \tag{7}$$

That is, $\mathbf{x} = \bar{\mathbf{x}}, \forall \mathbf{X} \in \partial\Omega_0$.

In fact, the above procedure is a multiscale version of the Hill–Mandel homogenization (Hill, 1972), and we can prove that the average deformation gradient in a cohesive zone is exactly the same as $\mathbf{F}^c$; i.e.,

$$< \mathbf{F} >_{\Omega_0} = \mathbf{F}^c \tag{8}$$

where $\mathbf{F}^c$ may be viewed as the coarse scale deformation gradient.

Substituting Eq. (5) into the definition of spatial average, we have

$$< \mathbf{F} >= \frac{1}{|\Omega_0|}\int\limits_{\Omega_0} \frac{\partial \mathbf{x}}{\partial \mathbf{X}} d\Omega = \frac{1}{|\Omega_0|}\int\limits_{\Omega_0} \left(\mathbf{F}^c + \frac{\partial \mathbf{u}^{'}}{\partial \mathbf{X}}\right) d\Omega \tag{9}$$

where Ω_0 denotes the volume of the cohesive zone.

Integration by parts and using Eq. (7),

$$\frac{1}{|\Omega_0|}\int_{\Omega_0}\frac{\partial \mathbf{u}'}{\partial \mathbf{X}}d\Omega = \frac{1}{|\Omega_0|}\int_{\partial\Omega_0}\mathbf{u}'\otimes\boldsymbol{\mathcal{N}}dS = 0$$

where $\boldsymbol{\mathcal{N}}$ are the out-normal of $\partial\Omega_0$. It is then straightforward to show that Eq. (8) holds.

In particular, if the coarse scale deformation field inside the cohesive zone is compatible with the uniform deformation field inside the bulk elements, the coarse scale deformation field can then be represented by an affine function of coordinates. Hence,

$$\bar{\mathbf{F}} =< \mathbf{F} >_{\Omega_0} = \mathbf{F}^c := \frac{\partial \bar{\mathbf{x}}}{\partial \mathbf{X}}\Big|_{\mathbf{x}\in\Omega} \tag{10}$$

Then we can determine the affine deformation map, $\bar{\mathbf{F}}^c$, if we know the finite-element nodal displacement. For example, in the case of plane strain, for a given finite-element method (FEM) nodal point along the boundary of the cohesive element, we have

$$\bar{x}_1 = a_1 + \bar{F}^c_{11}X_1 + \bar{F}^c_{12}X_2 \tag{11}$$

$$\bar{x}_2 = a_2 + \bar{F}^c_{21}X_1 + \bar{F}^c_{22}X_2 \tag{12}$$

$$\bar{x}_3 = a_3 + X_3 \tag{13}$$

where $\bar{F}^c_{ij}$ are constants.

Fixing the rigid body motion ($a_1 = a_2 = a_3 = 0$), one can easily determine the effective deformation gradient $\bar{\mathbf{F}}^c$ by using the information of FEM nodal displacements. For example, we can use the deformations of two diagonal lines of the cohesive zone, which can be expressed by the four FEM nodal displacements:

$$\mathbf{x}^+_{I+1} - \mathbf{x}^-_I = \bar{\mathbf{F}}^c\cdot(\mathbf{X}^+_{I+1} - \mathbf{X}^-_I), \text{ and } \mathbf{x}^+_I - \mathbf{x}^-_{I+1} = \bar{\mathbf{F}}^c\cdot(\mathbf{X}^+_I - \mathbf{X}^-_{I+1}) \tag{14}$$

to explicitly determine effective deformation gradient $\bar{\mathbf{F}}^c$ inside the cohesive zone as follows (see Fig. 1):

$$\begin{bmatrix}\bar{F}^c_{11}\\ \bar{F}^c_{12}\\ \bar{F}^c_{21}\\ \bar{F}^c_{22}\end{bmatrix} = \frac{1}{(bc-ad)}\begin{bmatrix}-d & 0 & b & 0\\ c & 0 & -a & 0\\ 0 & -d & 0 & b\\ 0 & c & 0 & -a\end{bmatrix}\begin{bmatrix}x^+_{I+1}-x^-_I\\ y^+_{I+1}-y^-_I\\ x^+_I - x^-_{I+1}\\ y^+_I - y^-_{I+1}\end{bmatrix} \tag{15}$$

where

$$a = X^+_{I+1} - X^-_I, \quad b = Y^+_{I+1} - Y^-_I, \quad c = X^+_I - X^-_{I+1}, \quad d = Y^+_I - Y^-_{I+1} \tag{16}$$

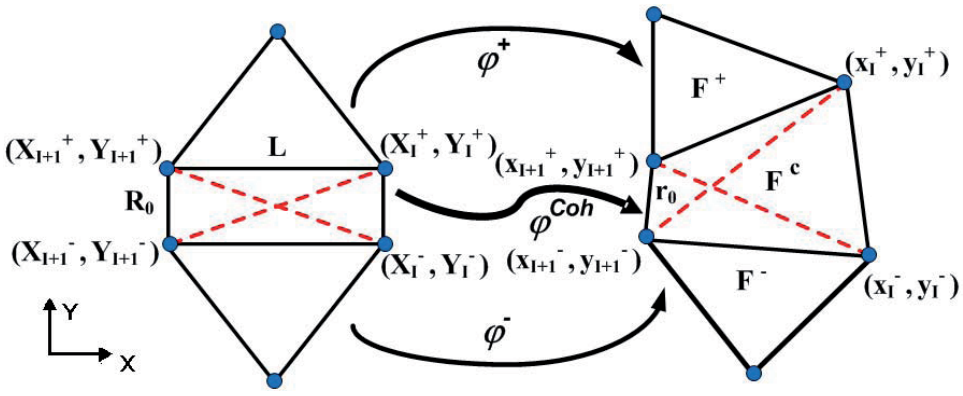

FIG. 1: Deformation gradient in cohesive zone.

2.3 Cauchy–Born Rule for Effective Field

In the proposed MCZM, to reduce the computational cost and complexity in computing the atomistic potential energy, the Cauchy–Born rule (Ericksen, 1984) has been adopted to calculate elastic energy in each element. The so-called Cauchy–Born assumes the deformation in each element is uniform, then the deformation gradient, $\mathbf{F}$, is constant in each element. Since in a given element e the deformation gradient, $\mathbf{F}_e$, is a constant tensor, an arbitrary deformed bond vector $\mathbf{r}_i$ in a unit cell in the element can be found by mapping the corresponding primitive Bravais lattice vector (i.e., the undeformed bond vector $\mathbf{R}_i$), into the deformed vectors,

$$\mathbf{r}_i = \mathbf{F}_e \mathbf{R}_i, \quad i = 1, 2, \cdots, n_b \tag{17}$$

where n_b is the total number of bonds in a unit cell.

Note that the bond vector $\mathbf{r}_i$ is the distance vector between the center atom in the unit cell to one of the atoms at the vertex of the unit cell. Taking the hexagonal lattice for example, if we only consider the nearest-neighbor interaction and there are six interatomic bond vectors. The deformed bond length is a function of deformation gradient of the element that the unit cell belongs to; i.e., $r_i = |\mathbf{r}_i| = r_i(\mathbf{F})$.

On the other hand, because the deformation in each element is uniform, we can calculate the elastic energy density in any given element by calculating the energy density of an arbitrary unit cell inside the element,

$$W_e = \frac{1}{\Omega_0^b} \sum_{i=1}^{n_b} \phi(r_i) = \frac{1}{\Omega_0^b} \sum_{i=1}^{n_b} \phi(\mathbf{F}_e \mathbf{R}_i) = W_e(\mathbf{F}_e), \quad e = 1, 2, \cdots, n_{\text{elem}} \tag{18}$$

where Ω_0^b is the volume of the unit cell in the referential configuration; $\phi(r_i)$ is the atomistic potential; and r_i, $i = 1, 2, \cdots, n_b$ is the current bond length for the ith bond in a unit cell. Note that superscript b indicates bulk, and Ω_0^b is the undeformed volume for the unit cell.

Consequently, the constitutive relations for the bulk medium can be established. For instance, the second Piola–Kirchhoff stress in the local QC method can be written in the following form:

$$\mathbf{S}(\mathbf{C}) = \frac{1}{\Omega_0^b} \sum_{i=1}^{n_b} \phi'(r_i) \frac{\partial r_i}{\partial \mathbf{C}} = \frac{1}{\Omega_0^b} \sum_{i=1}^{n_b} \frac{\partial \phi}{\partial r_i} \frac{\mathbf{R}_i \otimes \mathbf{R}_i}{r_i} \tag{19}$$

where $\mathbf{C} = \mathbf{F}^T \cdot \mathbf{F}$ is the right Cauchy–Green tensor. Similarly, we can find the first Piola–Kirchhoff stress tensor in each element as

$$\mathbf{P} = \mathbf{F}\mathbf{S} = \frac{1}{\Omega_0^b} \sum_{i=1}^{n_b} \frac{\partial \phi}{\partial r_i} \frac{\mathbf{r}_i \otimes \mathbf{R}_i}{r_i} \tag{20}$$

Since the deformation inside the bulk element is assumed to be uniform, we can then use the Cauchy–Born rule to establish the constitutive relation for the bulk elements, and this will provide us an atomistically enriched macroscale constitutive relation in multiscale computations.

This then provides us a means and justification to apply the Cauchy–Born rule to the mean field of interfacial cohesive zone; that is, the average of deformed lattice bond vector in each cohesive zone may be calculated as follows:

$$\bar{\mathbf{r}}_i = \bar{\mathbf{F}}^c \cdot \mathbf{R}_i, \quad i = 1, 2, \cdots, n_c \tag{21}$$

Subsequently, we can calculate the averaged first Piola–Kirchhoff stress tensor in each cohesive zone as

$$\bar{\mathbf{P}} = \frac{\partial W}{\partial \bar{\mathbf{F}}^c} = \frac{1}{\Omega_0^c} \sum_{i=1}^{n_c} \frac{\partial \phi_{\text{cohe}}}{\partial \bar{r}_i} \frac{\bar{\mathbf{r}}_i \otimes \mathbf{R}_i}{\bar{r}_i} \tag{22}$$

Therefore, in the proposed MCZM, we are making two coarse graining models: one for the bulk medium and another for the material interfaces, or defects. The beauty of such a coarse-grain procedure is that the effective deformation field inside the cohesive zone can be uniquely determined by the bulk finite-element nodal displacements, and

there is no finite-element (FE) interpolation inside the cohesive zone. The coarse-grain model for the cohesive zone is properly connected with the kinematics of bulk elements.

Without a coarse graining interface model, applications of the Cauchy–Born rule to FEM can only provide a coarse-grained model for bulk materials, and it cannot solve small-scale defect evolution problems. By constructing a finite-width cohesive zone and extending the Cauchy–Born rule to the coarse scale deformation field, the MCZM can simulate the overall behaviors of a nonuniform deformation caused by defects.

3. FEM IMPLEMENTATIONS

Based on the constitutive relations developed in the MCZM, we can compute the stress for each bulk element and in each cohesive zone. Once we obtain the stress information inside the cohesive zone, we can then find the cohesive traction forces along the boundaries of adjacent bulk elements as

$$\mathbf{T}^{\mathrm{cohe}} = \bar{\mathbf{P}} \cdot \boldsymbol{\mathcal{N}} \tag{23}$$

where $\boldsymbol{\mathcal{N}}$ is the out-normal of adjacent bulk FEs.

For a given bulk element, the Galerkin weak formulation of the MCZM can be derived as

$$\int_{B_0^e} \rho_0 \ddot{\varphi}^h \cdot \delta\varphi^h dV + \int_{B_0^e} \mathbf{P}(\varphi) : \delta\mathbf{F}^h dV - \int_{S_c^e} \mathbf{T}^{\mathrm{cohe}} \cdot \delta\varphi^h dS = \int_{B_0^e} \mathbf{B} \cdot \delta\varphi^h dV + \int_{\partial_t B_0^e} \bar{\mathbf{T}} \cdot \delta\varphi^h dS \tag{24}$$

where $\mathbf{B}$ is the body force; B_0^e is the eth element domain; $\partial_t B_0^e$ is the traction boundary of the element; and S_c^e is the cohesive boundary of the element.

Consider following linear FEM interpolation in each element,

$$\mathbf{u}^h(\mathbf{X}) = \sum_{I=1}^{n_{\mathrm{node}}} N_I(\mathbf{X}) \mathbf{d}_I \tag{25}$$

Following the standard FE discretization procedure (e.g., Hughes, 1987), we have the following discrete equations of motion:

$$\mathbf{M}\ddot{\mathbf{d}} + \mathbf{f}^{\mathrm{int}}(\mathbf{d}) - \mathbf{f}^{\mathrm{cohe}}(\mathbf{d}) = \mathbf{f}^{\mathrm{ext}} \tag{26}$$

where

$$\mathbf{M} = \mathop{\boldsymbol{A}}_{e=1}^{n_{\mathrm{elem}}} \int_{B_0^e} \rho_0 \mathbf{N}^{eT} \mathbf{N}^e dV \tag{27}$$

$$\mathbf{f}^{\mathrm{int}} = \mathop{\boldsymbol{A}}_{e=1}^{n_{\mathrm{elem}}} \int_{B_0^e} \mathbf{B}^{eT} \mathbf{P}^e(\mathbf{d}) dV \tag{28}$$

$$\mathbf{f}^{\mathrm{cohe}} = \mathop{\boldsymbol{A}}_{e=1}^{n_{\mathrm{elem}}} \int_{S_c^e} \mathbf{N}^{eT} \mathbf{T}_e^{\mathrm{cohe}} dS \tag{29}$$

$$\mathbf{f}^{\mathrm{ext}} = \mathop{\boldsymbol{A}}_{e=1}^{n_{\mathrm{elem}}} \left\{ \int_{B_0^e} \mathbf{N}^{eT} \mathbf{B}^e dV + \int_{\partial_t B_0^e} \mathbf{N}^{eT} \bar{\mathbf{T}}^e dS \right\} \tag{30}$$

where $\boldsymbol{A}$ is the element assemble operator, $\mathbf{N}^e$ is the element shape function matrix, and $\mathbf{B}^e$ is the element $\mathbf{B}$ matrix.

If the Newmark-β time integration method (with $\beta = 0$ and $\gamma = 0.5$) is used in the displacement update, we have

$$\mathbf{d}_{n+1} = \mathbf{d}_n + \mathbf{v}_n \Delta t_n + \frac{1}{2} \mathbf{a}_n (\Delta t_n)^2 \tag{31}$$

$$\mathbf{a}_{n+1} = \mathbf{M}^{-1}\left(\mathbf{f}^{\text{ext}} - \mathbf{f}^{\text{int}} + \mathbf{f}^{\text{cohe}}\right) \tag{32}$$

$$\mathbf{v}_{n+1} = \mathbf{v}_n + \frac{1}{2}\left(\mathbf{a}_n + \mathbf{a}_{n+1}\right)\Delta t_n \tag{33}$$

where $\mathbf{d}_n$ is the displacement field at time step n; $\mathbf{v}_n$ is the velocity field at time step n; and $\mathbf{a}_n$ is the acceleration field at time step n. The subscripts n and $n+1$ denote the quantities evaluated at time t_n and t_{n+1}. After the displacement field is updated, the deformation gradient in each bulk element can be subsequently updated as

$$\mathbf{F}_n^e = \mathbf{I} + \sum_{I=1}^{n_{\text{node}}} \mathbf{B}_I^e \mathbf{d}_n^e \tag{34}$$

and, subsequently, the stress measures can then be updated according to Eq. (38).

Similarly, the effective deformation gradient in each cohesive element can be also updated. For the case of plane strain, it is updated based on the following equations:

$$\begin{bmatrix} \bar{F}_{11}^c(t_n) \\ \bar{F}_{12}^c(t_n) \\ \bar{F}_{21}^c(t_n) \\ \bar{F}_{22}^c(t_n) \end{bmatrix} = \begin{bmatrix} 1 \\ 0 \\ 0 \\ 1 \end{bmatrix} + \frac{1}{2LR_0} \begin{bmatrix} -d & 0 & b & 0 \\ c & 0 & -a & 0 \\ 0 & -d & 0 & b \\ 0 & c & 0 & -a \end{bmatrix} \begin{bmatrix} u_{I+1}^+(t_n) - u_I^-(t_n) \\ v_{I+1}^+(t_n) - v_I^-(t_n) \\ u_I^+(t_n) - u_{I+1}^-(t_n) \\ v_I^+(t_n) - v_{I+1}^-(t_n) \end{bmatrix} \tag{35}$$

where $[u_I^{\pm}(t_n), v_I^{\pm}(t_n)] = \mathbf{d}_I^{\pm}(t_n)$, and the meaning of the superscripts $\pm$ is referred to Fig. 1 for their definitions; L is the side length of the adjacent bulk elements; and R_0 is the thickness of the cohesive element. The constants, a, b, c, d, are defined in Eq. (16). The stress inside the cohesive zone can then be updated by using Eq. (22). Here, R_0 is a physical parameter that is related to the characteristic length scale of specific defects considered. For instance, for composite modeling, this length scale should correspond to the actual interfacial width between the two phases, which is a measurable quantity. In the case of polycrystal, it should be the width of the grain boundary, which varies from case to case; and for single crystal, it should be the width of a typical persistent slip band, depending on which stage of failure that we are modeling. As an alternative, different length scales can be built in the MCZM by applying a newly developed multiresolution theory (see McVeigh et al., 2006; Vernerey et al., 2007, 2008; McVeigh and Liu, 2009).

4. MATERIAL COHESIVE LAW IN THE MIXED MODE

After obtaining the stress inside the cohesive zone, we can readily find the cohesive traction forces along the boundary of the cohesive zone, which is the same boundary of the adjacent bulk elements with the opposite out-normals:

$$\mathbf{T}^{\text{cohe}} = \mathbf{P}^c(\bar{\mathbf{F}}^c) \cdot \boldsymbol{\mathcal{N}} \tag{36}$$

where $\boldsymbol{\mathcal{N}}$ is the out-normal of adjacent bulk FEs. We can then find the relationships between the cohesive traction and corresponding opening displacements of the cohesive zone.

To demonstrate the process, we let the local coordinate X_1 parallel to the element mesh boundary be considered. We can then denote $\bar{u}$ as the relative effective horizonal (tangential) opening displacement, and $\bar{v}$ as the relative effective vertical (normal) opening displacement of the cohesive zone. Therefore, one may find that the traction along the element boundary is an explicit function of the effective deformation gradient inside the cohesive zone. For simplicity, we demonstrate this for the pair potential, for instance LJ potential, and the corresponding depletion potential. Consider the effective deformation gradient inside the cohesive zone for the cases of the pure Mode I and mixed mode are given separately as follows:

$$\bar{\mathbf{F}}_n = \begin{bmatrix} 1, & 0 \\ 0, & 1 + \bar{v}/R_0 \end{bmatrix} \quad \text{and} \quad \bar{\mathbf{F}}_m = \begin{bmatrix} 1, & \bar{u}/R_0 \\ 0, & 1 + \bar{v}/R_0 \end{bmatrix} \tag{37}$$

or $\bar{\mathbf{F}}_m(\boldsymbol{\Delta})$ in short. Note that R_0 is the width of the cohesive zone. Substituting the relations in Eq. (37) into Eq. (36), one can find the relationship between the element traction and the relative separation (opening displacements) of the cohesive zone:

$$\mathbf{T}^{\text{cohe}} = \mathbf{P}^c[\bar{\mathbf{F}}(\boldsymbol{\Delta})] \cdot \boldsymbol{\mathcal{N}}$$

Recall that the first Piola–Kirchhoff stress inside the cohesive zone may be written as

$$\mathbf{P}^c = \bar{\mathbf{F}}_m(\boldsymbol{\Delta})\mathbf{S}(\boldsymbol{\Delta}) = \frac{1}{\Omega_0^b}\sum_{i=1}^{n_b}\frac{\partial\phi}{\partial r_i}(\boldsymbol{\Delta})\frac{\mathbf{r}_i(\boldsymbol{\Delta})\otimes\mathbf{R}_i}{r_i(\boldsymbol{\Delta})} \tag{38}$$

This is because $\mathbf{r}_i = \bar{\mathbf{F}}_m(\boldsymbol{\Delta})\cdot\mathbf{R}_i$.

In Fig. 2, the cohesive laws of both the normal traction/Mode-I opening displacement and the mixed mode opening displacement are displayed, which are calculated based on Eqs. (36) and (37).

After we obtained the bulk potential and the depletion potential, we may construct a mesoscale cohesive zone potential as:

$$\phi_{\text{cohe}} = (1-\alpha)\phi_{\text{bulk}} + \alpha\phi_{\text{depl}}, \quad 0 \le \alpha \le 1 \tag{39}$$

where parameter α may depend on an internal variable, such as the von Mises stress; i.e., $\alpha = \alpha(\sigma_e)$. Initially, the bulk zone and the cohesive zone have the same bulk potential, which means initially $\alpha = 0$. Then, we may define the following simple criterion for α:

$$\alpha(\sigma_e) = \begin{cases} 0, & \text{if } \sigma_e < \sigma^* \\ 1, & \text{if } \sigma_e \ge \sigma^* \end{cases} \tag{40}$$

where σ^* is the material strength.

When the above criterion is met, α will switched from 0 to 1, and the cohesive law then will switch from the bulk potential to the depletion potential during the material failure process. This process is irreversible, because parameter α here plays a role of "internal variable" that is a state variable or damage variable.

A major advantage of the MCZM is that it can easily provide cohesive traction along the bulk element boundary for both normal and tangential traction from the same expression [Eq. (36)], whereas in the conventional cohesive FEM approach, these two traction laws are given separately, and they are not related to lattice structure or atomistic potential.

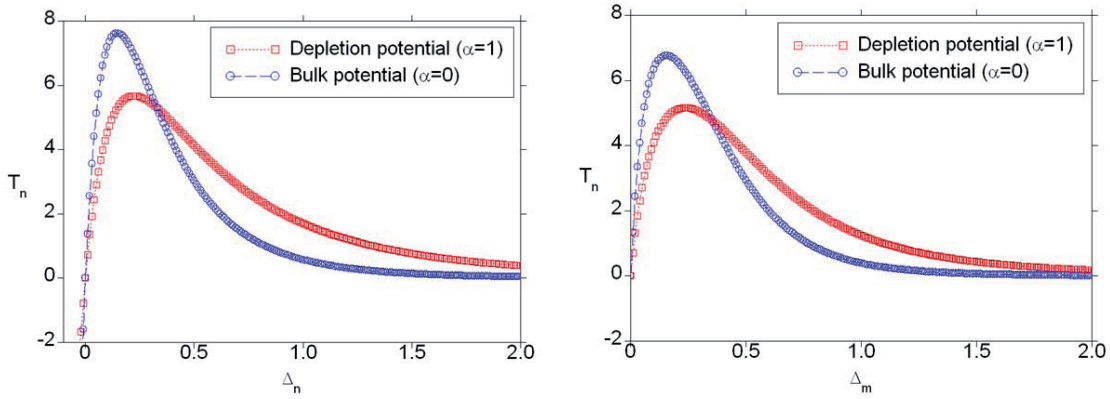

(a) (b)

FIG. 2: (a) cohesive normal traction vs. normal deformation and **(b)** cohesive normal traction vs. mixed deformation in cohesive zone.

5. MESH CONVERGENCE TEST

Generally, the results of the cohesive method are sensitive to its elements size. To test the effects of mesh size in the MCZM, a unilateral tension test is implemented with three different meshes. The test specimen is a two-dimensional (2D) plate with dimension (2000×2000). Constant velocity boundary condition is applied on both top and bottom edges. Hereby, three cases, which are corresponding to different mesh sizes, are employed as shown in Fig. 3. There is a small pre-crack in the left central region of the specimen. As a result, Fig. 4 shows the crack propagation in the specimen. It can be seen clearly that the crack propagates along the same path although the mesh density varies much more.

It is worthwhile to mention that if the cohesive zone has no thickness, there is a convergence problem as the conventional cohesive FEM suffers. This is where precisely this method excels, because between a pair of triangle elements, we have a finite-width cohesive zone element. More detailed discussion on mesh convergence can be found in Qian and Li (2011).

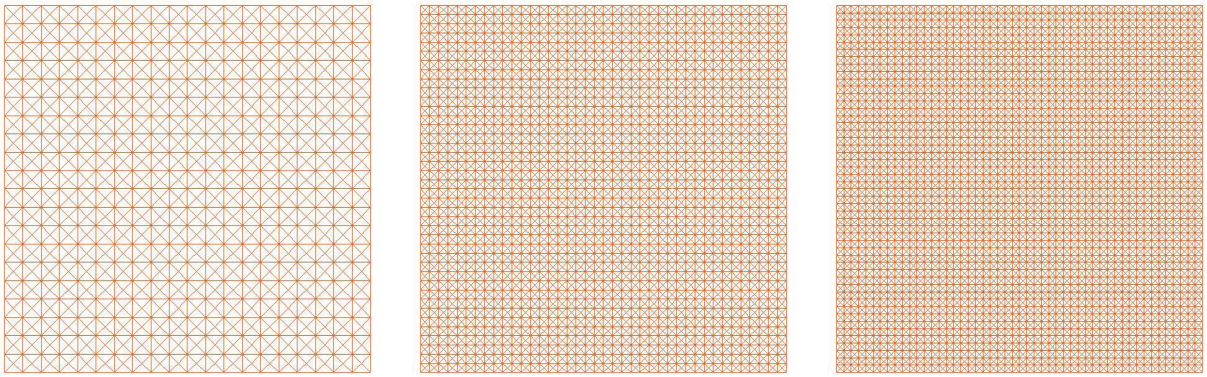

(a) (b) (c)

FIG. 3: Different mesh densities for crack propagation simulation: **(a)** Case 1 with 1,600 bulk elements; **(b)** Case 2 with 6,400 bulk elements; **(c)** Case 3 with 10,000 bulk elements.

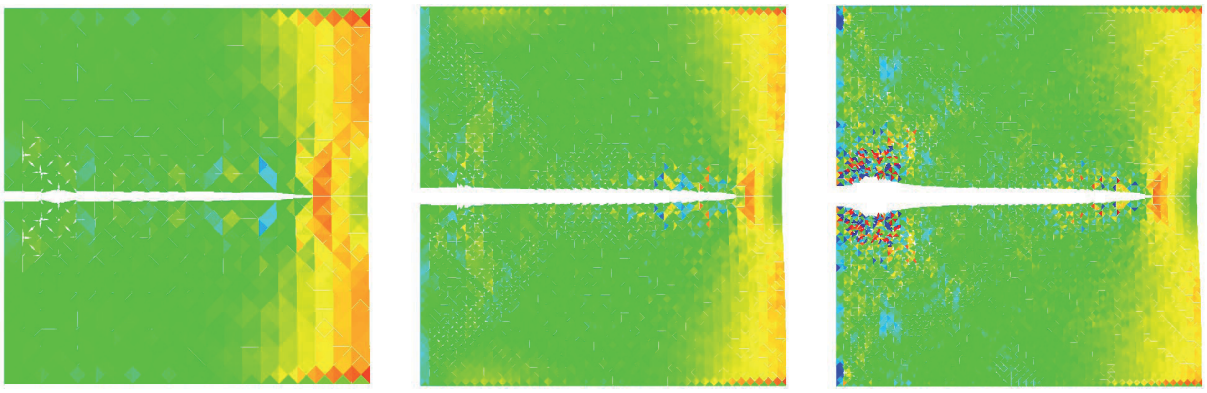

(a) (b) (c)

FIG. 4: Crack propagation for different mesh densities(stress contour): **(a)** Case 1; **(b)** Case 2; **(c)** Case 3.

6. NUMERICAL SIMULATIONS

6.1 Example I: Simulations of High-Speed Impact and Spall Fractures in Composite Materials

To validate the proposed MCZM, we have applied it to simulate a special dynamic fracture problem that has been thoroughly studied (Zeng and Li, 2010).

In this study, numerical simulations have been carried out to simulate high-speed impact-induced spall fractures in composite materials. The exact problem statement is described in Fig. 5. It is a rigid projectile impacting with a deformable plate. In the simulation, a 2D plate with dimension $(L_X \times L_Y = 8000 \times 3200)$ is under free boundary condition. There are 16,000 bulk elements used with the characteristic dimension of 20 $\sim$ 30 nm, and there are 23,860 cohesive zone elements used with the thickness of 5 atomic spacings. The specimen size in reduced units corresponds to micrometers in physical dimensions. The impact speed in the reduced unit is v = 0.64, corresponding to 100 m/s in physical dimensions. The time step in the Newmark-β integration method is chosen as Δt = 0.01. Contact problems are characterized by impenetrability conditions that need to be enforced during computation. We adopted the exact enforcement of the impenetrability condition in a single time step (see Hughes et al., 1976).

In the composite materials model, there are seven reinforced rims along vertical direction and four along the horizontal direction with rim width L_R = 320. The cohesive strength in the reinforced rims (zone "Mat1") is $\sigma_{\mathrm{mat1}} = \sigma^*$. We assume cohesive strength in cohesive zone "Mat2" is weaker than "Mat1" with cohesive strength $\sigma_{\mathrm{mat2}} = 0.3\sigma^*$. We also assume that cohesive strength in interface zone "Mat3" is the weakest zone in the specimen with strength $\sigma_{\mathrm{mat3}} = 0.1\sigma^*$.

A time sequence of the fracture process is shown in Fig. 6. After the initial impact, the compressive stress wave starts to propagate from the contact surface to the opposite boundary, when the stress wave reached the boundary, it will change from a compressive stress wave to a tensile stress wave, and propagates back to the initial impact surface. The reflected shock wave has long been identified as the main mechanism that causes the so-called spall fracture. In Fig. 6, the phenomena of spall fracture due to impact loads are captured. From Fig. 7, one can find that first the fracture starts from the horizontal interfacial cohesive zone, the cracks then propagate along the horizontal direction to reach the reinforced rims, and then the crack starts to climb along the vertical interfacial zone [see Fig. 7(b) for a zoom-in view of the right corner of the specimen].

For comparison purposes, we changed the cohesive strength in interface zone "Mat3" to $\sigma_{\mathrm{mat3}} = 0.4\sigma^*$, and we assume that cohesive strength in cohesive zone "Mat2" is the weakest zone in the specimen with strength $\sigma_{\mathrm{mat2}} = 0.1\sigma^*$. A time sequence of the fracture process is shown in Fig. 8. Different from the first simulation, one can find that

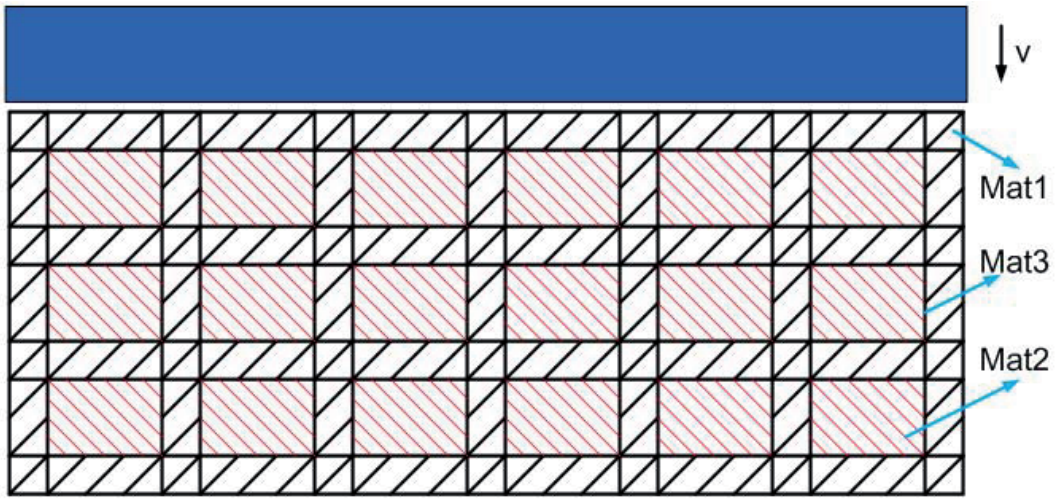

FIG. 5: The statement of the impact problem.

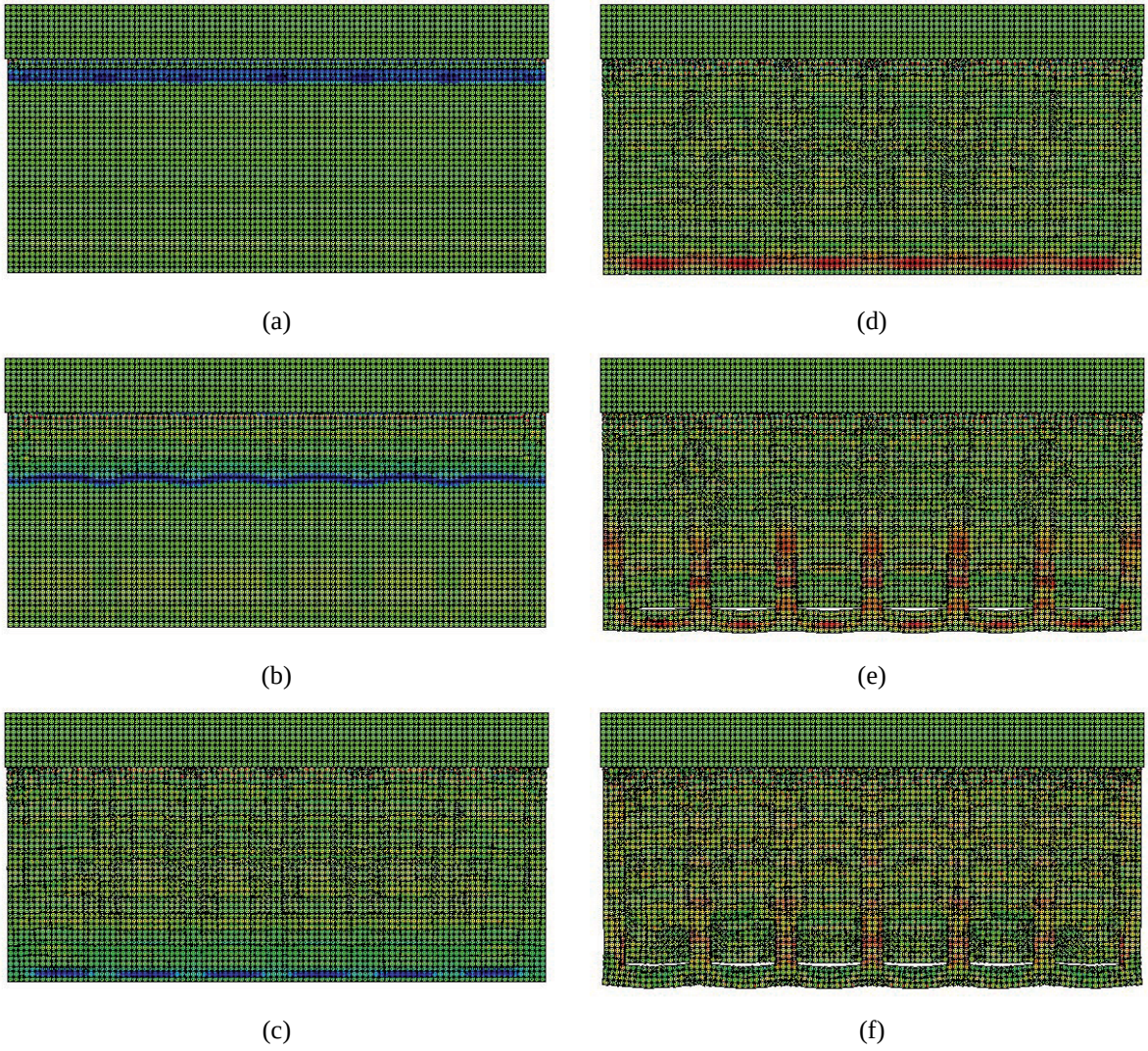

(a) (d)

(b) (e)

(c) (f)

FIG. 6: Case 1: Time sequence of a high speed impact induced spall fracture in composite materials.

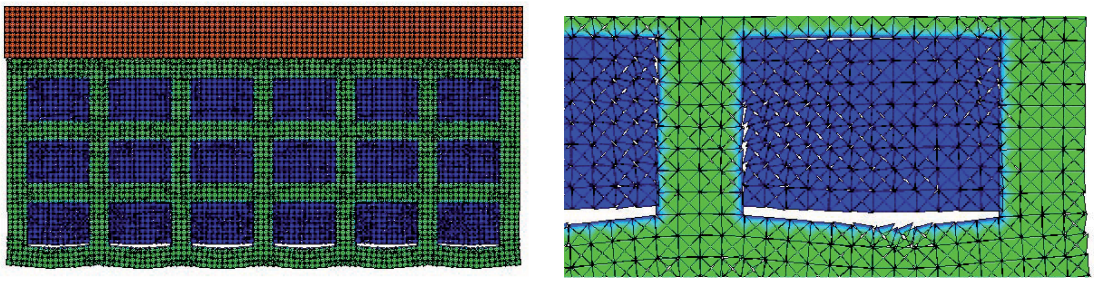

(a) (b)

FIG. 7: Case 1: High speed impact induced spall fracture in composite materials.

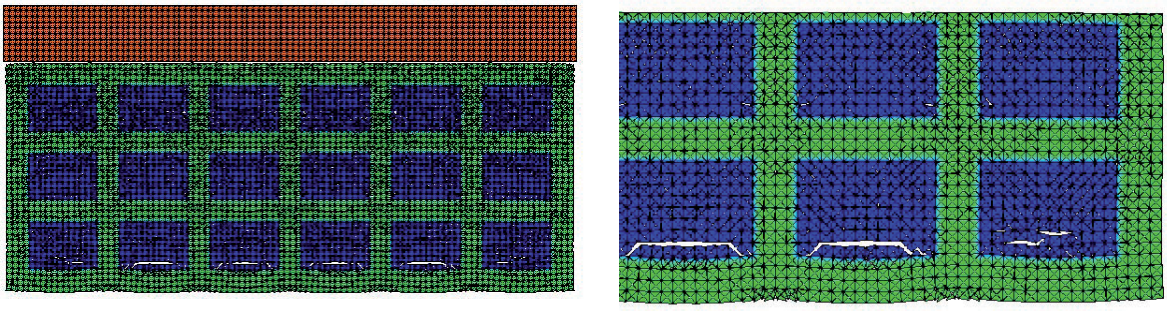

(a) (b)

FIG. 8: Case 2: High speed impact induced spall fracture in composite materials.

the fracture starts from the horizontal cohesive zone in "Mat2" because it is now the weakest zone in the specimen; subsequently, the fracture starts to shear along a 45 degree angled line, and it finally reaches the interlaminar interface and then the interface starts debonding.

6.2 Example II. Simulations of Different Fracture Patterns in Composite Materials with Defects

To further illustrate the versatility of the model, numerical simulations have been carried out to simulate the fracture process in composite materials with defects. In the simulation, a 2D plate with dimension ($L_X \times L_Y$ = 8000 $\times$ 3200) is under dynamically prescribed uniaxial tension load. There are 16,000 bulk elements and 23,860 cohesive zone elements.

The cohesive strength in the reinforced rims (zone "Mat1") is $\sigma_{\mathrm{mat1}} = \sigma^*$. There are 4 cohesive elements with defect strength $\sigma_{\mathrm{defect}} = 0.02\sigma^*$, which are much weaker than the regular cohesive elements (zone "Mat2") with mechanical strength $\sigma_{\mathrm{mat2}} = 0.4\sigma^*$; the interfacial cohesive elements (zone "Mat3") have the same mechanical strength as the regular cohesive elements with $\sigma_{\mathrm{mat3}} = 0.4\sigma^*$.

We designed two simulations for comparison purposes. In the first simulation, the reinforced rims are all along the specimen boundary with rim width L_R = 480; in the second simulation, we add two more reinforced rims with one along the central vertical direction and another along the central horizontal direction.

The time sequences of the fracture process for the two simulations are shown in Figs. 9 and 10, respectively. For both simulations, the fractures start to grow around the defects. The phenomena of crack initiation, nucleation, growth, and coalescence are captured from the simulations. The differences between these two simulations are that for the first case, the two horizontal cracks will coalescence to become one big crack; however, in the second case, when the two horizontal cracks reach the vertical rims the material starts to debond along the interfacial elements. Those simulations can enhance our understanding of interfacial debonding and decohesion in the bi-material interface and may provide help in composite materials design.

7. DISCUSSIONS AND CONCLUSIONS

Composite materials bring together the individual properties of physically different phases or components with the aim of creating a material that shows new and superior properties compared to the individual components. In order to maximize the ability of the composite materials it is necessary to develop reliable and accurate simulation techniques to predict the behaviors of composites in operation. Most of composite materials have multiscale properties by design. Multiscale prediction for physical and mechanical parameters of composite materials, including materials with periodic configurations and materials with random defect distributions, has become a central issue in simulation-based technology. The focal point of the current research is multiscale simulations for fracture, localized softening and/or strengthen, and micro-structural evolution of materials and mechanical systems.

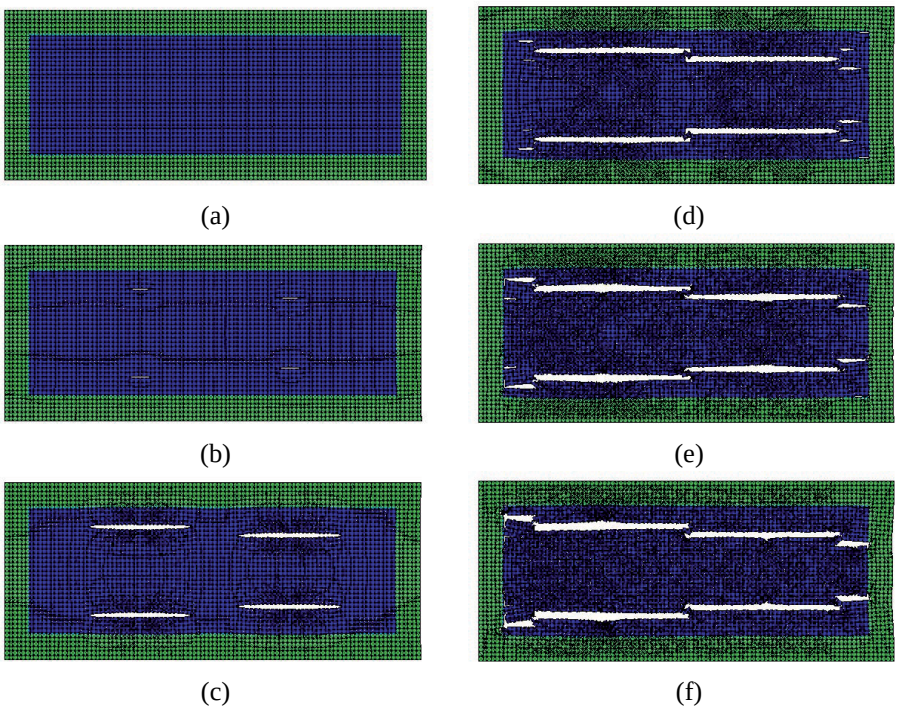

FIG. 9: Case 1: Time sequence of fracture process in composite materials with defects.

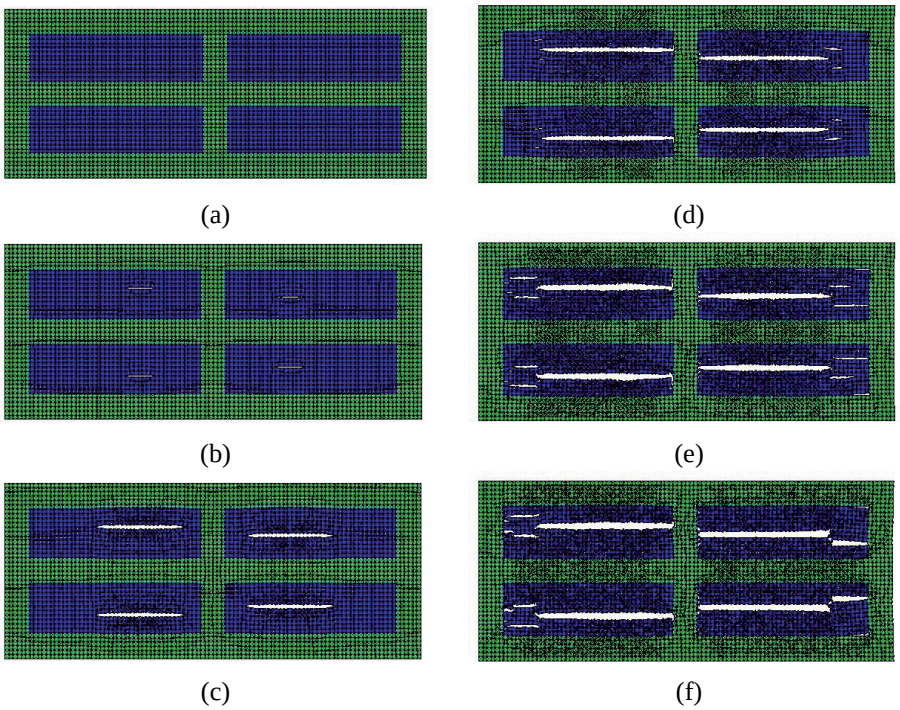

FIG. 10: Case 2: Time sequence of fracture process in composite materials with defects.

In this paper, we have applied a recently developed MCZM to study the possibility of using atomistic information to extrapolate constitutive information of both bulk materials as well as composite interfaces in order to precisely study the responses of composite materials under impact loads and to quantitatively simulate the failure mechanism and fracture patterns in composite materials. This method is capable of simulating strong discontinuities across a solid at the nanoscale, such as micro-cracks and dislocations at small scales. Compared to the conventional cohesive finite element method, the proposed cohesive zone model is a multiscale model that employs the basic principles of colloidal physics and surface chemistry to determine the interface cohesive force, and it exploits the underneath atomistic structure to construct surface or interface cohesive laws. By using the MCZM, we have successfully described both bulk and interface material properties of a given composite material/structure at the mesoscale, and simulate the possible failure mechanisms that may happen during impact loads. By doing so, we have demonstrated the potential of the MCZM as a major modeling and simulation technique in both composite material modeling as well as multiscale simulations in general. The main point of this paper is to demonstrate the applicability of the proposed multiscale cohesive zone method by applying a simple LJ potential. To solve realistic engineering problems, we are working on an embedded atom cohesive zone model, in which an EAM-type potential is used to extrapolate both bulk and interface cohesive material properties. This work will be reported in a separate paper.

ACKNOWLEDGMENTS

This work is supported by a grant from NSF (Grant No. CMMI-0800744) and a grant from the Army Research Office, which are greatly appreciated.

REFERENCES

Alfaro, M. V., Suiker, A. S. J., de Borst, R., and Remmers, J. J. C., Analysis of fracture and delamination in laminates using 3D numerical modelling, *Eng. Fract. Mech.*, vol. **76**, pp. 761–780, 2009.

Alfaro, M. V., Suiker, A. S. J., Verhoosel, C. V., and de Borst, R., Numerical homogenization of cracking processes in thin fibre-epoxy layers, *Eur. J. Mech. A/Solids*, vol. **29**, pp. 119–131, 2010.

Barenblatt, G. I., The mathematical theory of equilibrium of cracks in brittle fracture, *Adv. Appl. Mech.*, vol. **7**, pp. 55–129, 1962.

Braides, A., Lew, A. J., and Ortiz, M., Effective cohesive behavior of layers of interatomic planes, *Arch. Ration. Mech. Anal.*, vol. **180**, pp. 151–182, 2006.

Daw, M. S. and Baskes, M. I., Embedded-atom method: Derivation and application to impurities, surfaces, and other defects in metals, *Phys. Rev. B*, vol. **29**, pp. 6443–6453, 1984.

Dugdale, D. S., Yielding of steel sheets containing slits, *J. Mech. Phys. Solids*, vol. **8**, pp. 100–104, 1960.

Ericksen, J. L., The Cauchy and Born hypotheses for crystals, in *Phase Transformations and Material Instabilities in Solids*, ed., Gurtin, M. E., pp. 61–77, New York: Academic, 1984.

Geers, M. G. D., Kouznetsova, V. G., and Brekelmans, W. A. M., Multi-scale computational homogenization: Trends and challenges, *J. Comput. Appl. Math.*, vol. **234**, pp. 2175–2182, 2010.

Hayes, R. L., Ortiz, M., and Carter, E. A., Universal binding-energy relation for crystals that accounts for surface relaxation, *Phys. Rev. B*, vol. **69**, p. 172104-1–172104-4, 2004.

Hill, R., On constitutive macro-variables for heterogeneous solids at finite strain, *Proc. R. Soc. London, Ser. A*, vol. **326**, pp. 131–147, 1972.

Hilleborg, A., Modeer, M., and Petersson, P. E., Analysis of crack formation and crack growth in concrete by fracture mechanics and finite elements, *Cement Concr. Res.*, vol. **6**, pp. 773–782, 1976.

Hirschberger, C. B., Ricker, S., Steinmann, P., and Sukumar, N., Computational multiscale modelling of heterogeneous material layers, *Eng. Fract. Mech.*, vol. **76**, pp. 793–812, 2009.

Hughes, T. J. R., Talor, R., Sackman, J., Curnier, A., and Kamoknukulchai, W., A finite element method for a class of contact-impact problem, *Comput. Methods Appl. Mech. Eng.*, vol. **8**, pp. 249–276, 1976.

Hughes, T. J. R., *The Finite Element Method: Linear Static and Dynamic Finite Element Analysis*, Englewoods Cliffs, NJ: Prentice Hall, 1987.

Israelachvili, J., *Intermolecular & Surface Forces*, 2nd ed., New York: Academic Press, 1992.

Matous, K., Kulkarnib, M. G., and Geubelleb, P. H., Multiscale cohesive failure modeling of heterogeneous adhesives, *J. Mech. Phys. Solids*, vol. **56**, pp. 1511–1533, 2008.

McVeigh, C., Vernerey, F., Liu, W. K., and Brinson, L. C., Multiresolution analysis of material design, *Comput. Methods Appl. Mech. Eng.*, vol. **195**, pp. 5053–5076, 2006.

McVeigh, C. and Liu, W. K., Multiresolution modeling of ductile reinforced brittle composites, *J. Mech. Phys. Solids*, vol. **57**, pp. 244–267, 2009.

Nguyen, O. and Ortiz, M., Coarse-graining and renormalization of atomistic binding relations and universal macroscopic cohesive behavior, *J. Mech. Phys. Solids*, vol. **50**, pp. 1727–1741, 2002.

Park, K., Paulino, G. H., and Roesler, J. R., A unified potential-based cohesive model of mixed-mode fracture, *J. Mech. Phys. Solids*, vol. **57**, pp. 891–908, 2009.

Qian, J. and Li, S., Application of multiscale cohesive zone model to simulate fracture in polycrystalline solids, *ASME J. Eng. Mater. Technol.*, vol. **133**, article No. 011010,1-10, 2011.

Samimi, M., van Dommelen, J. A. W., and Geers, M. G. D., An enriched cohesive zone model for delamination in brittle interfaces, *Int. J. Numer. Methods Eng.*, vol. **80**, pp. 609–630, 2009.

Vernerey, F., Liu, W. K., and Moran, B., Multiscale micromorphic theory for hierarchical materials, *J. Mech. Phys. Solids*, vol. **55**, pp. 2603–2651, 2007.

Vernerey, F., Liu, W. K., Moran, B., and Olson, G. B., A Micromorphic model for the multiple scale failure of heterogeneous materials, *J. Mech. Phys. Solids*, vol. **56**, pp. 1320–1347, 2008.

Xu, X.-P. and Needleman, A., Numerical simulations of fast crack growth in brittle solids, *J. Mech. Phys. Solids*, vol. **42**, pp. 1397–1434, 1994.

Zeng, X. and Li, S., A multiscale cohesive zone model and simulations of fractures, *Comput. Methods Appl. Mech. Eng.*, vol. **199**, pp. 547–556, 2010.